ADVANCED FUNCTIONAL MATERIALS

Supporting Information

for *Adv. Funct. Mater.,* DOI: 10.1002/adfm.202112276

On the Origin of Seebeck Coefficient Inversion in Highly Doped Conducting Polymers

Kai Xu, Tero-Petri Ruoko, Morteza Shokrani, Dorothea Scheunemann, Hassan Abdalla, Hengda Sun, Chi-Yuan Yang, Yuttapoom Puttisong, Nagesh B. Kolhe, José Silvestre Mendoza Figueroa, Jonas O. Pedersen, Thomas Ederth, Weimin M. Chen, Magnus Berggren, Samson A. Jenekhe, Daniele Fazzi, Martijn Kemerink,* and Simone Fabiano**

Supporting Information

On the origin of Seebeck coefficient inversion in highly electrochemically doped conducting polymers

Kai Xu†, Tero-Petri Ruoko†, Morteza Shokrani, Dorothea Scheunemann, Hassan Abdalla, Hengda Sun, Chi-Yuan Yang, Yuttapoom Puttisong, Nagesh B. Kolhe, José Silvestre Mendoza Figueroa, Jonas O. Pedersen, Thomas Ederth, Weimin M. Chen, Magnus Berggren, Samson A. Jenekhe, Daniele Fazzi, Martijn Kemerink*, Simone Fabiano**

K. Xu[+], T.-P. Ruoko[++], H. Sun[+++], C.-Y. Yang, M. Berggren, S. Fabiano
Laboratory of Organic Electronics, Department of Science and Technology, Linköping University, SE-60174 Norrköping, Sweden
E-mail: simone.fabiano@liu.se

M. Berggren, S. Fabiano
Wallenberg Wood Science Center, Linköping University, SE-60174 Norrköping, Sweden

M. Berggren, S. Fabiano
n-Ink AB, Teknikringen 7, SE-58330 Linköping, Sweden

M. Shokrani, D. Scheunemann, M. Kemerink
Center for Advanced Materials, Heidelberg University, Heidelberg, Germany
E-mail: martijn.kemerink@cam.uni-heidelberg.de

H. Abdalla, Y. Puttisong, W. M. Chen, M. Kemerink
Division of Electronics and Photonic Materials, Department of Physics, Chemistry and Biology, Linköping University, Linköping, Sweden

N. B. Kolhe, S. A. Jenekhe
Department of Chemical Engineering and Department of Chemistry, University of Washington, 98195 Seattle, WA, USA

J. S. Mendoza Figueroa, J. O. Pedersen, T. Ederth
Division of Biophysics and Bioengineering, Department of Physics, Chemistry and Biology, Linköping University, SE-58183 Linköping, Sweden

D. Fazzi[++++]
Institute of Physical Chemistry, University of Cologne, Cologne, Germany
E-mail: daniele.fazzi@unibo.it

[+]Current address: State Key Laboratory of Metastable Materials Science and Technology, Yanshan University, Qinhuangdao, China

[++]Current address: Smart Photonic Materials, Faculty of Engineering and Natural Sciences, Tampere University, Tampere, Finland

[+++]Current address: State key Laboratory for Modification of Chemical Fibers and Polymer Materials, Donghua University, Shanghai, China

[++++]Current address: Unviersità di Bologna, Dipartimento di Chimica "Giacomo Ciamician", via F. Selmi, 2, 40126 Bologna, Italy

†These authors contributed equally to this work

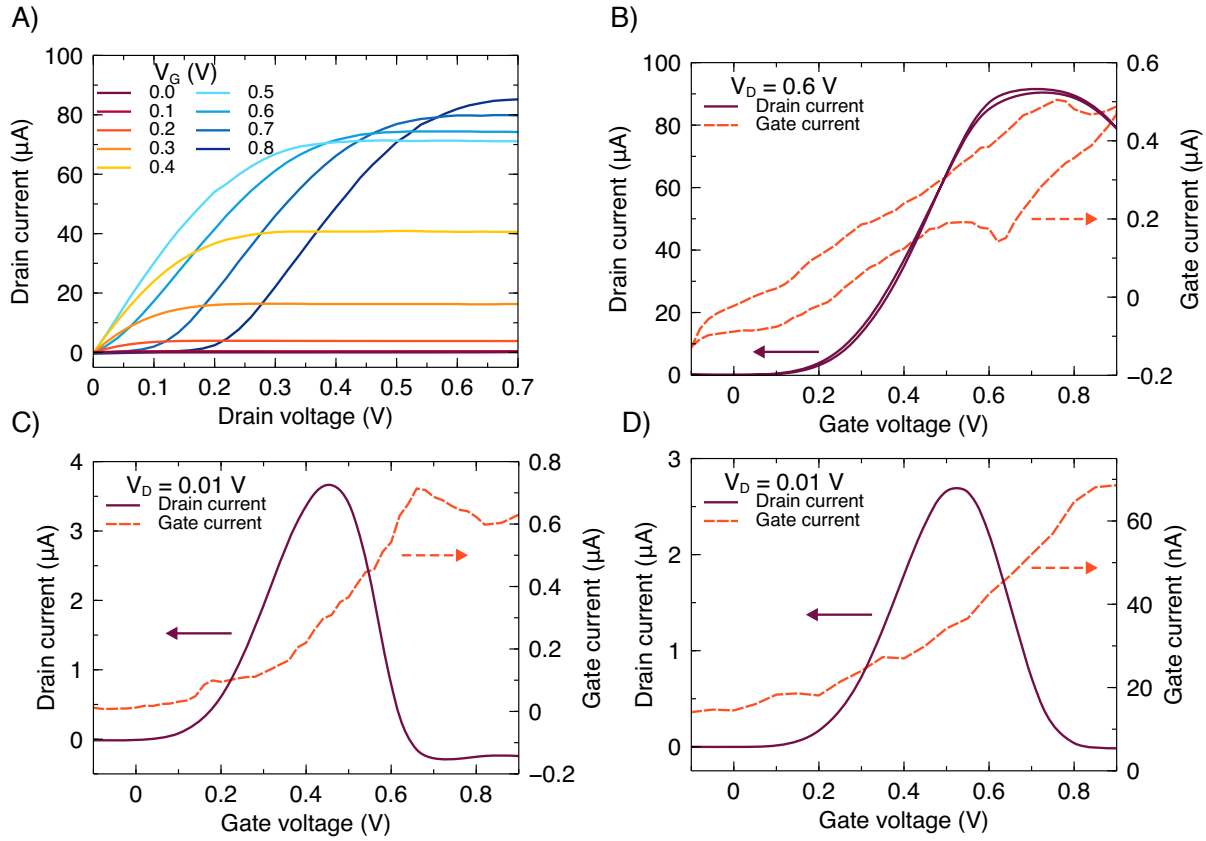

Figure S1. Electrical characterization of BBL based organic electrochemical transistor. (*A*) Output curves at different gate voltages. (*B*) Transfer curve and gate current at V_D = 0.6 V. Transfer curves and gate currents at V_D = 0.01 V with a pristine (*C*) and partially dried (*D*) gel electrolyte.

Although the polymer surface area is large (2 mm by 10 mm, with thickness approximately 60 nm) and gold electrodes (1 mm by 10 mm) were used, the gate current is relatively small and can be neglected for V_D = 0.6 V. However, for low drain voltages (i.e., V_D = 0.01 V for conductivity measurements) the gate leakage current becomes significant at $V_G > 0.6$ V and $V_G < 0.2$ V. However, using a partially dried gel electrolyte decreases the gate leakage dramatically with only small changes to the transfer characteristics. To elucidate the origin of the drain current onset shift at $V_G > 0.6$ V, we performed *in-situ* spectroscopic characterization of the OECT channel using UV-Vis transmission and Raman microspectroscopies (see Figure S12). Both measurements clearly indicate that the BBL channel is more doped closer to the source. This allows us to show that the negative transconductance of BBL-based OECTs at high applied gate voltages is caused by doping the channel to such a high degree that multiply charged states, which we observe spectroscopically to begin forming at 0.5–0.6 V, cause the formation of a weakly conducting region close to the source terminal. As the gate voltage further increases,

the weakly conducting region becomes wider due to extending the higher degree of doping further along the channel towards the drain terminal, while simultaneously decreasing the conductivity closer to the source. This effectively pinches off the conductivity of the channel at the source terminal, resulting in the apparent drain current onset voltage shift in Figure S1A and the negative transconductance at high gate voltages.

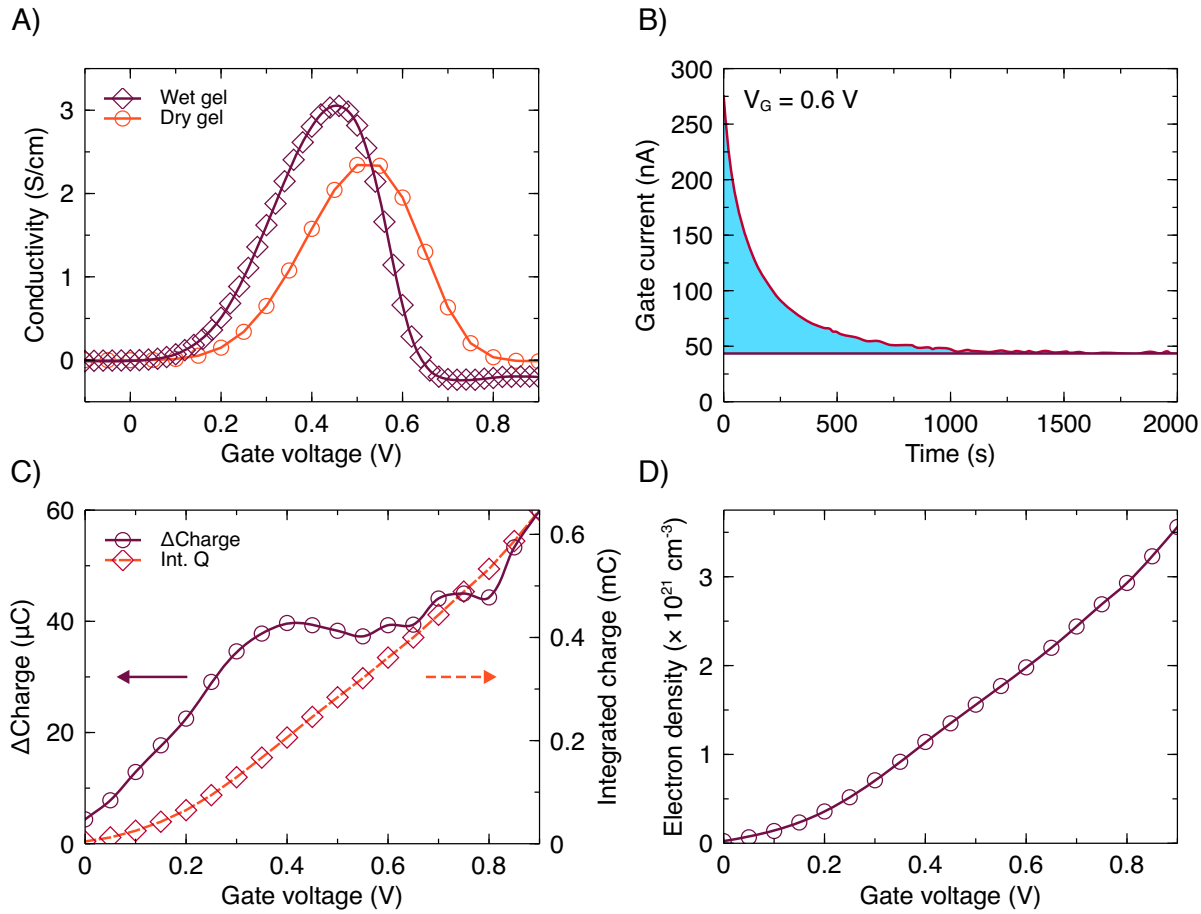

Figure S2. Electrical characterization and charge integration of a BBL-based OECT with a dried PSSNa gel electrolyte. In all cases V_D = 0.01 V. (*A*) Conductivities of the BBL channel obtained with wet and partially dried gel electrolytes. (*B*) Example of integration of the charge transferred to the BBL film. (*C*) Change in charges and integrated total charge transferred to the BBL film. (*D*) Calculated electron density for the whole channel volume.

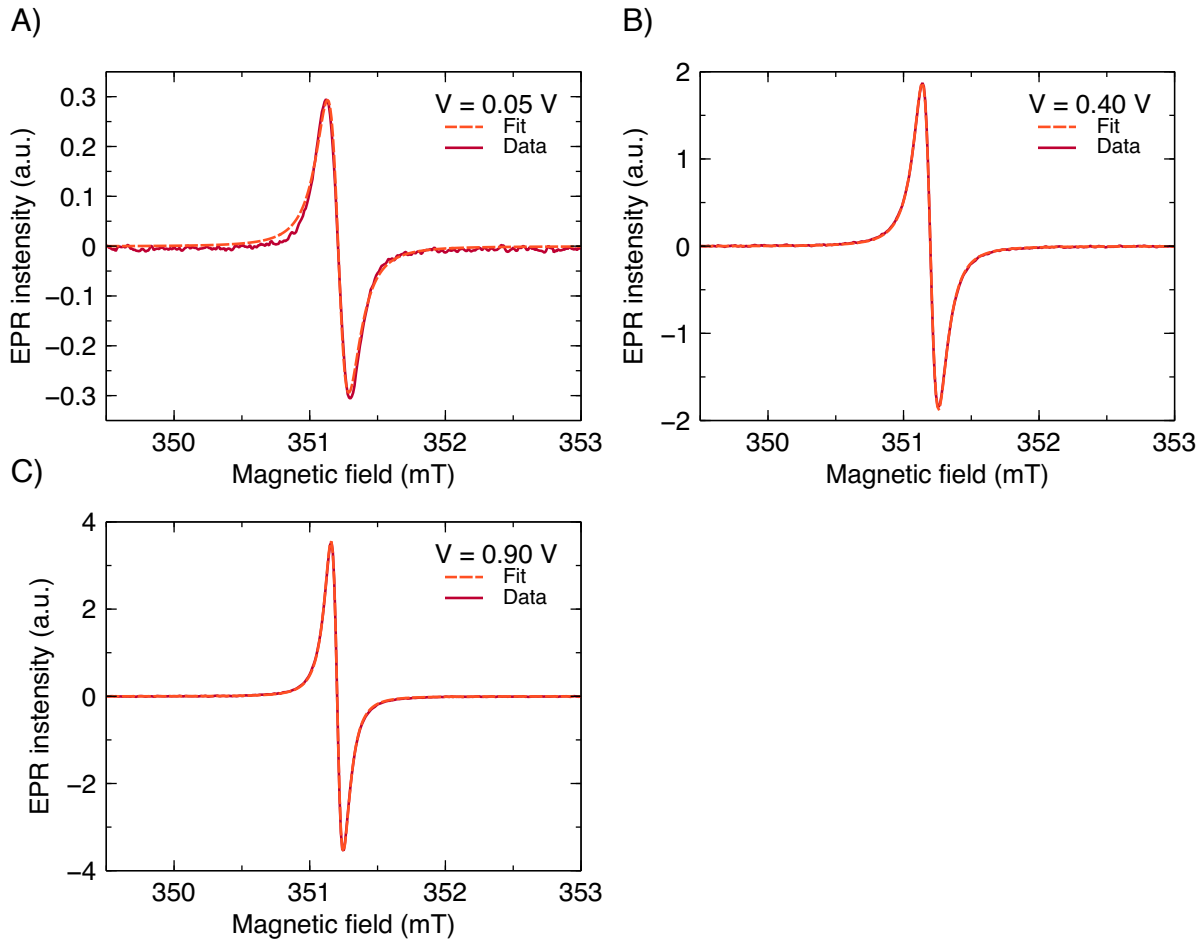

Figure S3. EPR spectra and corresponding Lorentzian fits at (*A*) 0.05 V, (*B*) 0.40 V, and (*C*) 0.90 V applied voltage.

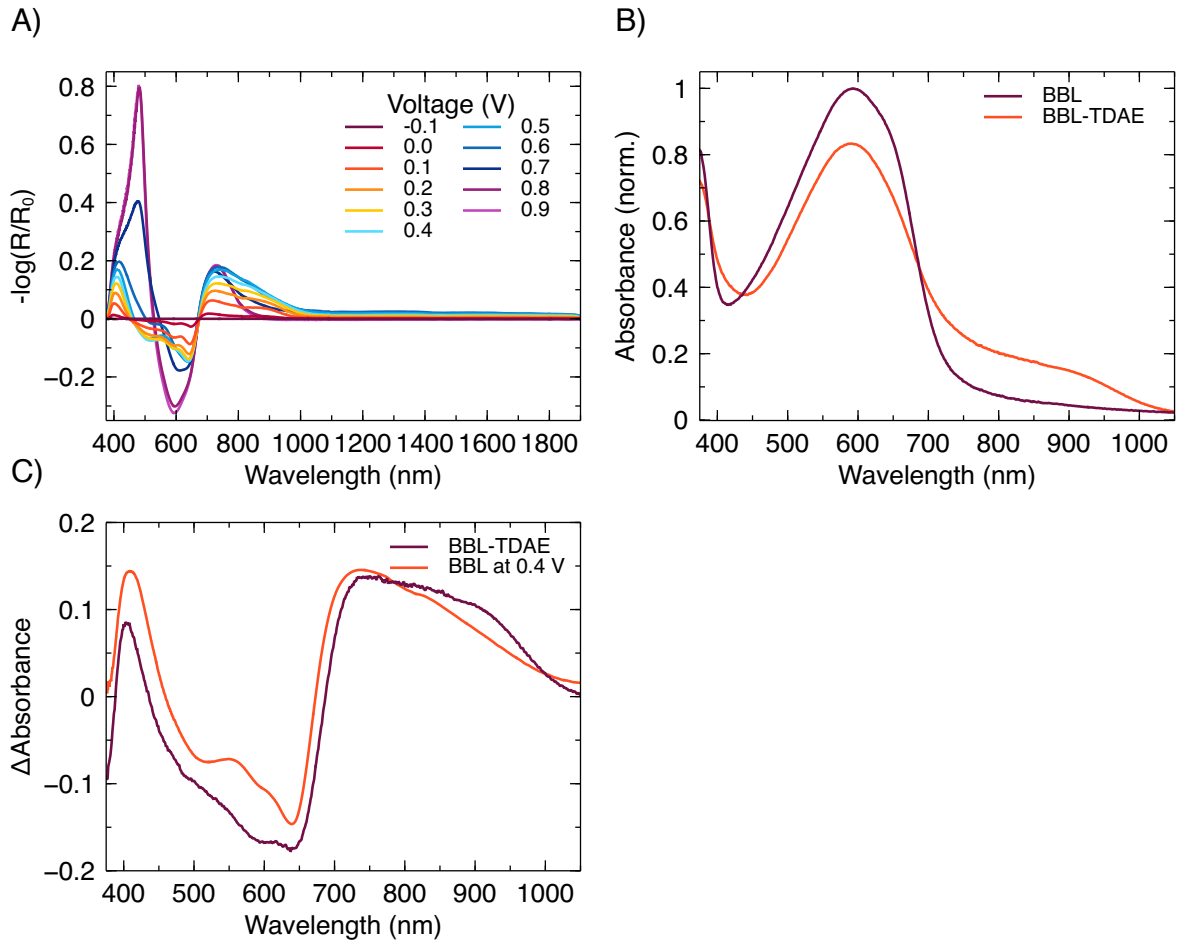

Figure S4. (*A*) *In-situ* UV-Vis difference absorption spectra measured in reflectance mode. The baseline measurement was the same BBL film kept at -0.1 V applied voltage (straight line) to dedope the film prior to measuring the difference spectra. (*B*) Normalized UV-Vis absorption spectra of pristine BBL and the relative absorption spectrum of the same film chemically doped with TDAE. (*C*) Comparison of the difference absorption spectra between BBL-TDAE and pristine BBL as well as the difference spectrum of BBL electrochemically doped at 0.4 V.

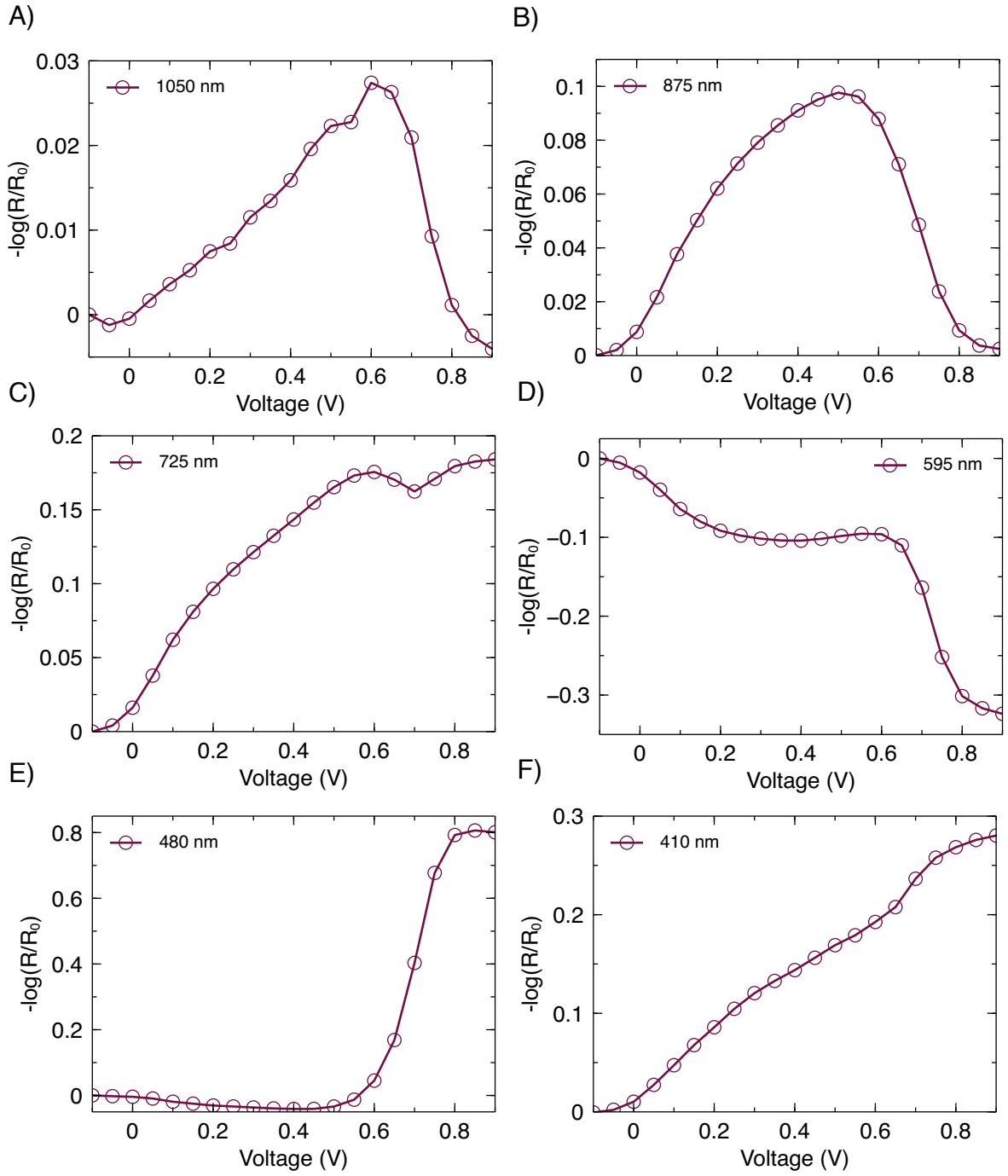

Figure S5. *In-situ* UV-Vis difference absorption at selected wavelengths measured in reflectance mode. The baseline measurement was the same BBL film kept at -0.1 V applied voltage to dedope the film prior to measuring the difference spectra.

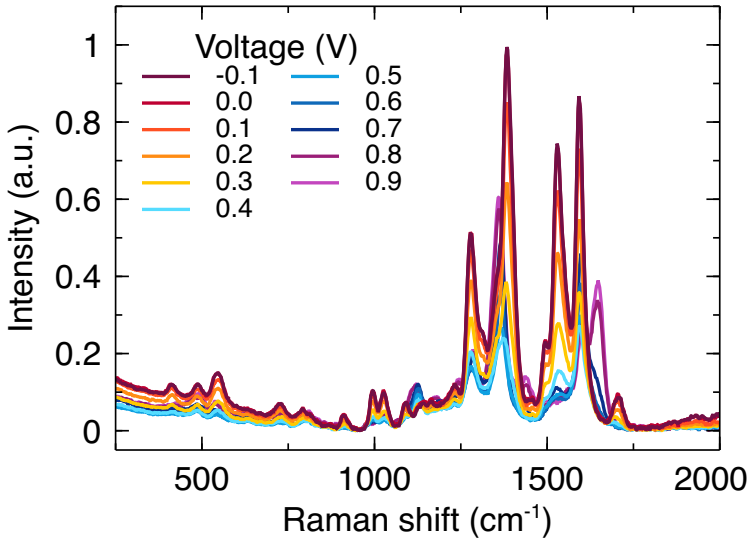

Figure S6. *In-situ* Raman spectra of BBL with 532 nm excitation in the range 250–2000 cm^{-1}. Raman measurements were performed of BBL films on top of gold covered glass substrates with doctor bladed PSSNa electrolyte and the Ag/AgCl pellet gate electrode positioned away from the illuminated area.

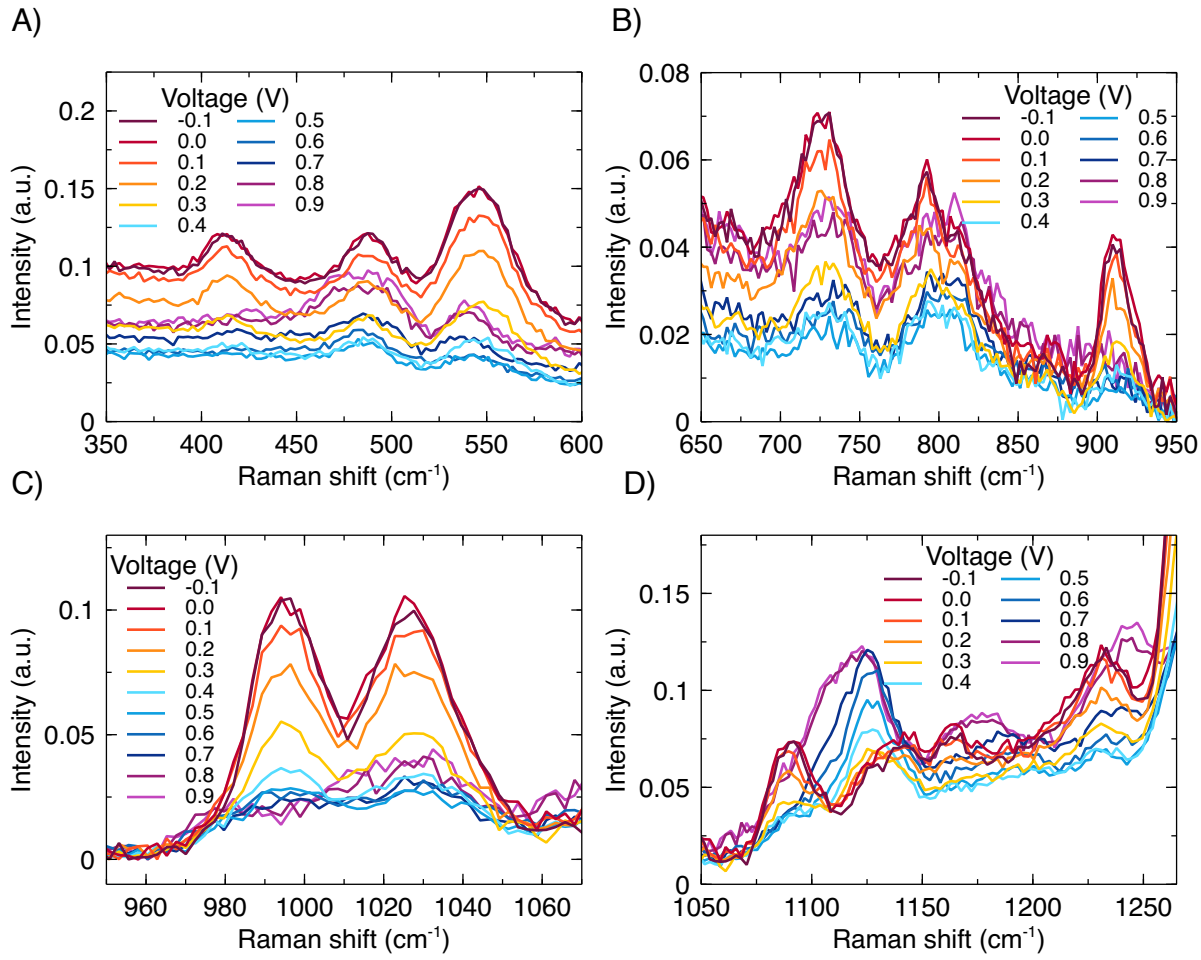

Figure S7. *In-situ* Raman spectra of BBL with 532 nm excitation in the ranges (*A*) 350–600 cm^{-1}, (*B*) 650–950 cm^{-1}, (*C*) 950–1070 cm^{-1}, and (*D*) 1050–1265 cm^{-1}. Raman measurements were performed of BBL films on top of gold covered glass substrates with doctor bladed PSSNa electrolyte and the Ag/AgCl pellet gate electrode positioned away from the illuminated area.

The naphthalene (994 cm^{-1}) and imidazole (1025 cm^{-1}) ring breathing as well as the C-H twisting (909 cm^{-1}) vibrations decrease drastically by 0.5 V and remain at the same level at higher gate voltages Similarly, the aromatic modes at 408, 487, and 545 cm^{-1} as well as the imidazole ring breathing vibrations at 725 and 792 cm^{-1} also gradually decrease by 0.5 V, followed by a slight increase with the peaks remaining at the same position. On the other hand, the C-H bending vibrations at 1089, 1141, 1165, and 1230 cm^{-1} are gradually decreased in a similar fashion, but higher gate voltages lead to gradual increases at different positions, with new peaks forming at 1120 and 1245 cm^{-1}.

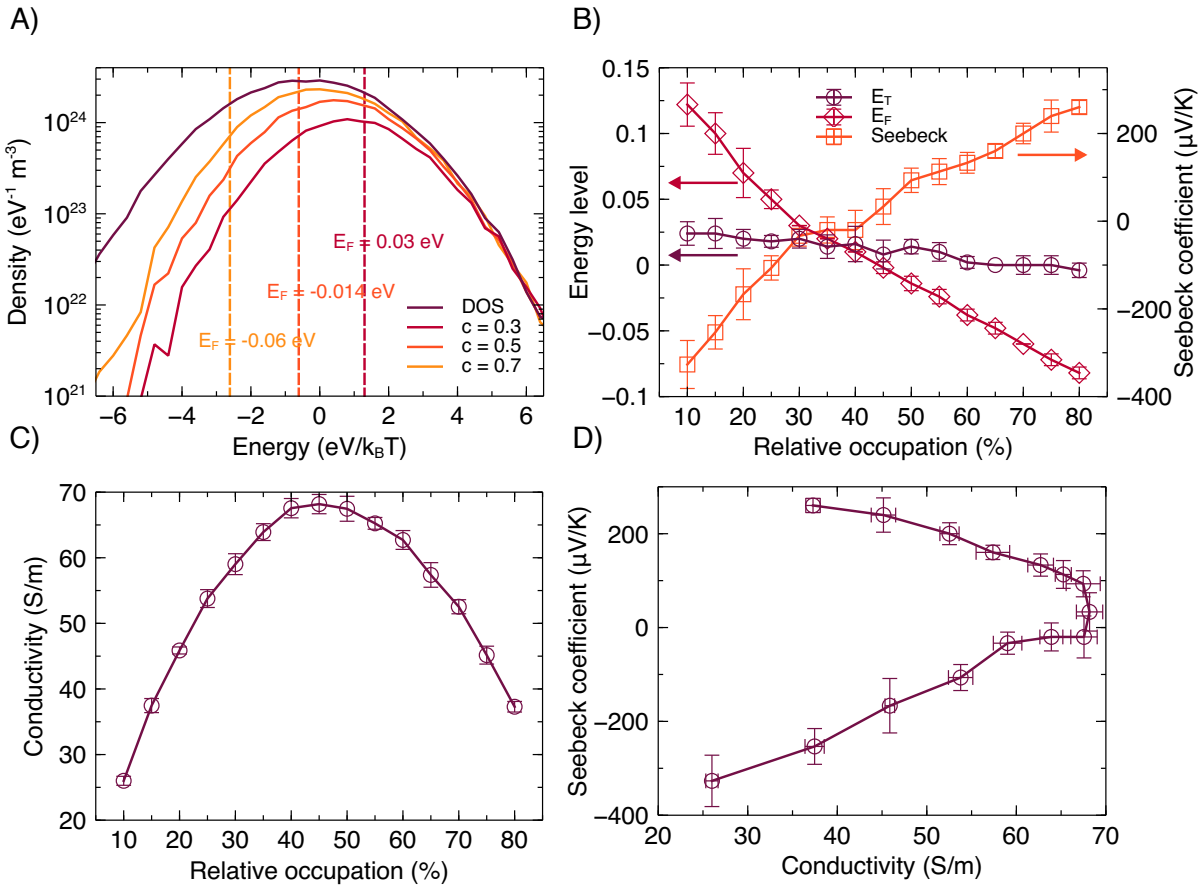

Figure S8. To show the generality of Seebeck inversion effect in a hopping model and for contrast with the more complex kMC model used in the main text, a simple kMC calculation is performed on a 20×20×20 grid with lattice constant $a_{NN} = 3$ nm without considering Coulomb interactions and assuming one electron can only occupy a single site, with the results averaged over 5 samples. (*A*) Gaussian shaped DOS and DOOS at different relative occupation (c = 0.3, 0.5, 0.7). (*B*) Transport energy E_t, Fermi energy E_f, and Seebeck coefficient with increasing relative occupation. (*C*) Conductivity with increasing relative occupation. (*D*) Seebeck coefficient versus conductivity.

Comparison of panels B and C shows that also in the naïve state-filling model for non-interacting particles, the Seebeck coefficient changes sign as the electrical conductivity reaches a maximum, which matches with both experimental data and the more complex kMC model used in the main text. Note that increasing the doping concentration leads to inter-charge carrier Coulomb energies in the order of 10–100 meV at higher doping concentrations. These values are comparable with the energetic disorder in the material, and as a result they have a considerable effect on the charge transport in the system as discussed in the main text.

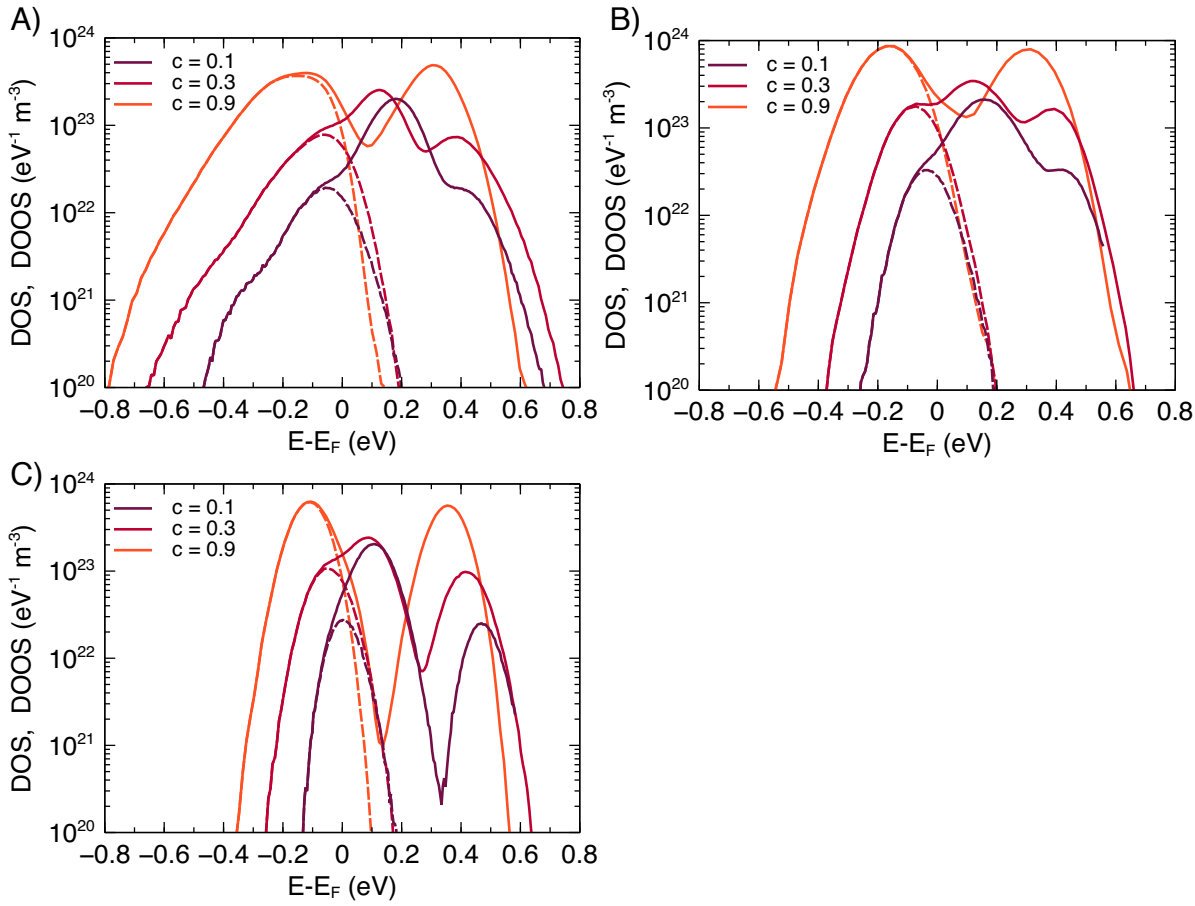

Figure S9. Calculated DOS and DOOS for an initial DOS that is (*A*) exponential, (*B*) Gaussian and (*C*) rectangular, all with respect to the Fermi energy for relative occupations of 10 %, 30 % and 90 % at a_{NN}=3 nm. In all cases, a hard Coulomb gap opens around the Fermi energy at high charge carrier concentrations.

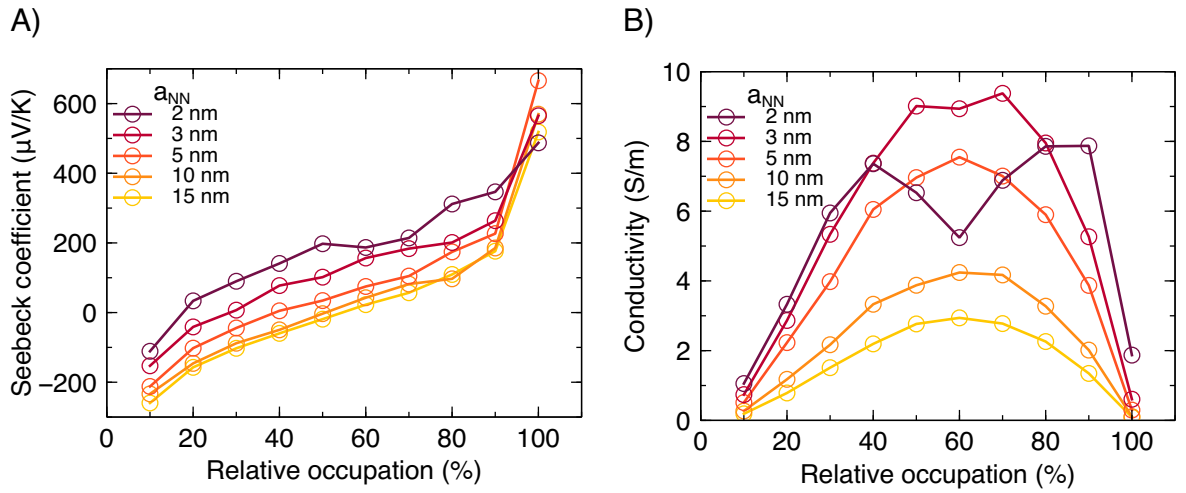

Figure S10. Variation of (*A*) Seebeck coefficient and (*B*) Electrical conductivity versus relative occupation for different lattice constants a_{NN}. Otherwise, the same input parameters as in Figure 4 of the main text are used.

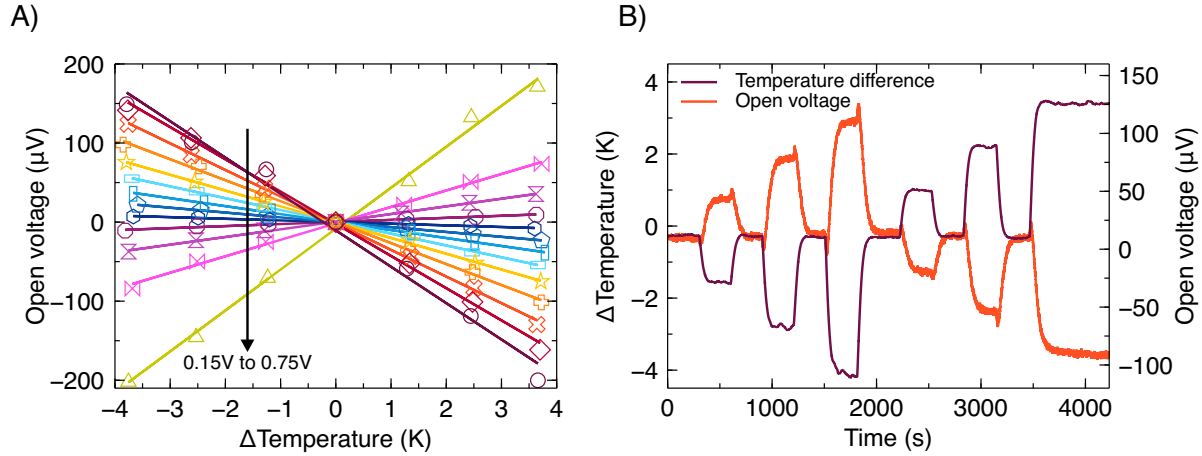

Figure S11. (*A*) Open voltages of the BBL-based OECT as a function of temperature difference at different gate voltages used to determine the Seebeck coefficient. (*B*) Temperature difference between the Peltier modules in the Seebeck coefficient measurement and open voltages of the BBL-based OECT as a function of time at V_G = 0.3 V.

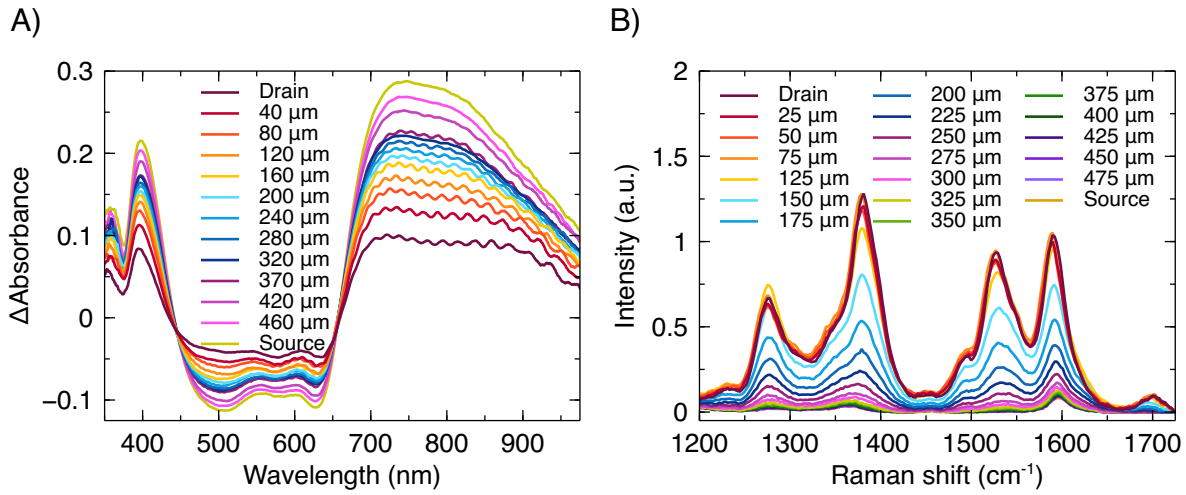

Figure S12. *In-situ* UV-Vis and Raman microspectroscopy of a BBL OECT channel. (*A*) difference UV-Vis absorption spectra measured in transmission mode and (*B*) Raman spectra from inside the channel of a BBL-based OECT, illustrated schematically in Fig 1A. The distances in the legend illustrate distance from drain towards source. Both measurements were performed with $V_D = V_G = 0.5$ V.

DFT calculations

All DFT calculations were performed *via* an oligomer approach. Each structure was optimized by using the hybrid range-separated-corrected DFT functional, namely ωB97X-D combined with double-zeta (and in some cases triple-zeta) split valence polarized Pope's basis set 6-31G* (6-311G*). The choice of ωB97X-D3 was due to its well-known superior performance in describing charged and excited states in conjugated polymers.[1-3] The effects of considering either B3LYP or a double hybrid DFT functional (e.g., B2PLYP), as well as an augmented basis set (e.g., 6-311+G*), were tested previously.[4,5] Results did not show improvements with respect to the ωB97X-D/6-31G* approach, and similar conclusions regarding the DFT wavefunction instability in describing multiply charged states can be drawn.

The electronic states investigated here for BBL_4 were the neutral ground state (q = 0e) and the multi-charged states. In particular we considered:

a) the single negatively charged state (q = -1e, corresponding to 0.25 eru), which shows a doublet state spin multiplicity (D);

b) the double charged state (q = -2e, 0.50eru), that can be either a singlet (S) or a triplet (T) state;

c) the triple charged state (q = -3e, 0.75 eru), being either a doublet (D) or a quartet (Q);

d) q = -4e, 1eru, being either a singlet (S), triplet (T), or quintet (Qui);

e) q = -5e, 1.25 eru, for which we have considered a D or a Q state;

f) q = -6e, 1.50 eru, for which we have considered a S or a T state;

g) q = -7e, 1.75 eru, for which we have considered a D or a Q state;

h) q = -8e, 2.00eru, being a S, T, Qui, sextet (Sex) or nonet (N) state.

Multiply charged states were initially described using either the RDFT or UDFT approach, depending on their close or open-shell spin state. For each case, a wavefunction stability check was performed adopting the broken-symmetry (BS-UDFT) scheme (4, 5). If an instability in the wavefunction was found, both the electronic and nuclear structures were re-optimized following the BS-UDFT potential energy surface. All calculations were performed with the program package Gaussian16 C.01 (5). Further details about the BS-UDFT approaches and results can be found in our previous publications, namely Refs. 4 and 5.

For each charged state, all spin state multiplicities mentioned above were computed to be within the range of a few meV, being therefore accessible via thermal excitations.

The computed energy differences between spin states for each charged species are reported below (BS refers to broken symmetry solution) (DFT: wB97X-D/6-31G*):

- q = -2e, 0.50eru, Δ(T – S-BS) = -1.9x10^{-6} eV, **triplet** state more stable;
- q = -3e, 0.75eru, Δ(D-BS – Q-BS) = -1.3x10^{-4} eV, **doublet** state more stable;
- q = -4e, 1.00eru, Δ(T – S-BS) = -8.2x10^{-3} eV and Δ(Q – T) = -8.2x10^{-3} eV, **quintet** and **triplet** state degenerate;
- q = -5e, 1.25 eru, Δ(D – Q) = -2.7x10^{-1} eV, **doublet** more stable;
- q = -6e, 1.50eru, Δ(T – S-BS) = -6.7x10^{-3} eV, **triplet** more stable;
- q = -7e, 1.75eru, Δ(D – Q) = -2x10^{-2} eV, **doublet** more stable;
- q = -8e, 2.00eru, Δ(T – S) = -1 eV, Δ(N – S) ~ -1 eV **triplet** and **nonet** more stable.

FOD analysis (with def2-TZVP basis set) were performed by using ORCA v 4.2.1. All charged BBL_4 species show N_{FOD} larger than 1.00, thus showing strong static correlation effect playing in the electronic structure. TD-DFT calculations were performed at the same level of theory (wB97X-D/6-31G* or 6-311G*) and each spin-state multiplicity was considered.

References

1. U. Salzner and A. Aydin, *J. Chem. Theory Comput.*, **2011**, *7*, 2568–2583.

2. R. Baer, E. Livshits and U. Salzner, *Annu. Rev. Phys. Chem.*, **2010**, *61*, 85–109.

3. U. Salzner, *Wiley Interdiscip. Rev.: Comput. Mol. Sci.*, **2014**, *4*, 601–622.

4. D. Fazzi, et al., *J. Mater. Chem. C*, **2019**, *7*, 12876-12885.
5. D. Fazzi, et al., *Adv. Electron. Mater*., **2021**, *7*, 2000786.
6. M. J. Frisch, G. W. Trucks, H. B. Schlegel, G. E. Scuseria, M. A. Robb, J. R. Cheeseman, G. Scalmani, V. Barone, G. A. Petersson, H. Nakatsuji, X. Li, M. Caricato, A. V. Marenich, J. Bloino, B. G. Janesko, R. Gomperts, B. Mennucci, H. P. Hratchian, J. V. Ortiz, A. F. Izmaylov, J. L. Sonnenberg, D. Williams-Young, F. Ding, F. Lipparini, F. Egidi, J. Goings, B. Peng, A. Petrone, T. Henderson, D. Ranasinghe, V. G. Zakrzewski, J. Gao, N. Rega, G. Zheng, W. Liang, M. Hada, M. Ehara, K. Toyota, R. Fukuda, J. Hasegawa, M. Ishida, T. Nakajima, Y. Honda, O. Kitao, H. Nakai, T. Vreven, K. Throssell, J. A. Montgomery, Jr., J. E. Peralta, F. Ogliaro, M. J. Bearpark, J. J. Heyd, E. N. Brothers, K. N. Kudin, V. N. Staroverov, T. A. Keith, R. Kobayashi, J. Normand, K. Raghavachari, A. P. Rendell, J. C. Burant, S. S. Iyengar, J. Tomasi, M. Cossi, J. M. Millam, M. Klene, C. Adamo, R. Cammi, J. W. Ochterski, R. L. Martin, K. Morokuma, O. Farkas, J. B. Foresman and D. J. Fox, Gaussian 16, Revision B.01, Gaussian, Inc., Wallingford CT, **2016**.